Chemical Engineering Journal 375 (2019) 121991

Contents lists available at ScienceDirect

Chemical Engineering Journal

journal homepage: www.elsevier.com/locate/cej

Facile construction of hierarchical flower-like Z-scheme $AgBr/Bi_2WO_6$ photocatalysts for effective removal of tetracycline: Degradation pathways and mechanism

Danlian Huang[a,b,*], Jing Li[a,b], Guangming Zeng[a,b,*], Wenjing Xue[a,b], Sha Chen[a,b], Zhihao Li[a,b], Rui Deng[a,b], Yang Yang[a,b], Min Cheng[a,b]

[a] College of Environmental Science and Engineering, Hunan University, Changsha 410082, PR China
[b] Key Laboratory of Environmental Biology and Pollution Control, Hunan University, Ministry of Education, Changsha 410082, PR China

HIGHLIGHTS

- Z-scheme $AgBr/Bi_2WO_6$ composites featuring Ag NPs electron mediator were fabricated.
- $AgBr/Bi_2WO_6$ composites exhibited superior photocatalytic activity for TC degradation.
- Ag NPs endowed the superior transfer and separation of photogenerated carriers.
- Z-scheme charge transfer mechanism enhanced the redox ability.
- Photocatalytic mechanism and degradation pathway of TC were revealed.

GRAPHICAL ABSTRACT

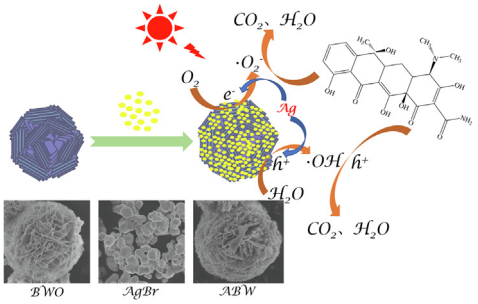

ARTICLE INFO

Keywords:
Flower-like Bi_2WO_6
Ag NPs
Z-scheme
Tetracycline
Degradation mechanism

ABSTRACT

A novel hierarchical flower-like $AgBr/Bi_2WO_6$ Z-scheme photocatalyst was prepared through the simplified hydrothermal and deposition-precipitation method. The as-prepared photocatalysts exhibited excellent photocatalytic performance for tetracycline (TC) degradation. Especially, AgBr (20 wt%)/Bi_2WO_6 displayed the optimal TC removal efficiency (87.5%) within 60 min of visible light illumination. Besides, no obvious decrease in photocatalytic performance was observed after four cycles. The excellent photocatalytic performance could be ascribed to the synergistic effect between electron mediator Ag nanoparticles (Ag NPs) and Z-scheme heterojunction charge transfer mechanism, which enhanced the light harvest capability, separation efficiency of photogenerated carriers and redox ability. Moreover, three-dimensional excitation-emission matrix fluorescence spectroscopy (3D EEMs) and liquid chromatography-mass spectrometry (LC-MS) analyses shed light on the mineralization behavior and the detailed decomposition pathway of TC. This work opened up a new road to efficient Z-scheme heterojunction design and provided novel insights into antibiotics elimination mechanism in photocatalysis.

* Corresponding authors at: College of Environmental Science and Engineering, Hunan University, Changsha 410082, PR China
E-mail addresses: huangdanlian@hnu.edu.cn (D. Huang), zgming@hnu.edu.cn (G. Zeng).

https://doi.org/10.1016/j.cej.2019.121991
Received 15 March 2019; Received in revised form 8 June 2019; Accepted 16 June 2019
Available online 17 June 2019
1385-8947/

1. Introduction

The increasing environmental pollution seriously threatened the development of human society [1–8] and numerous technologies were developed to remove pollutants from the environment [9–16]. Photocatalysis technology had aroused widespread concern in environmental remediation due to its green and available traits [17–19]. Nevertheless, the most common semiconductor TiO_2 could only be excited by ultraviolet light, which restricted its practical application thus brought challenge to the exploration of new visible-light-driven semiconductor photocatalysts [20–22].

Bismuth tungstate (Bi_2WO_6), the simplest member of the Aurivillius oxide family, had been highlighted for the visible photocatalytic activity. However, single Bi_2WO_6 still had a poor photocatalytic performance due to the fast recombination of photogenerated carriers and the unsatisfied optical absorption capacity. Generally, there were two ways to boost the photocatalytic performance of Bi_2WO_6. Firstly, morphology optimization of Bi_2WO_6. Based on different synthesis methods and conditions, the obtained materials expressed different dimensional morphologies with diverse specific surface areas [23,24], among which, hierarchical self-assembly superstructures presented the better degradation performance due to the larger specific surface area [25]. A great quantity of researches related to hierarchical flower-like Bi_2WO_6 had been reported, such as CdS QDs/Bi_2WO_6 [26], Bi_2WO_6/$BiPO_4$ [25] and g-C_3N_4/RGO/Bi_2WO_6 [27], which exhibited superior photocatalytic performance for various pollutants. The larger specific surface area endowed the pollutant molecules more active sites. Furthermore, the hierarchical flower-like structure of Bi_2WO_6 extended the transmission path of visible light and advanced the light harvesting capacity by scattering and diffusing light inside the structure [28]. Secondly, heterojunction construction of Bi_2WO_6. There were three heterojunction types: conventional heterojunction (type-I, type-II and type-III), p-n heterojunction and Z-scheme heterojunction [29,30]. Conventional type-I and type-III heterojunction were unfavorable for photocatalysis because electrons and holes accumulated in the same semiconductor and couldn't be separated owing to the staggered bandgap, respectively. Moreover, type-II and p-n heterojunction couldn't avoid the defect of declined redox ability because electrons and holes accumulated in lower reduction and oxidation potentials, respectively [30]. In contrast to the ways of heterojunction construction above, Z-scheme heterojunction photocatalyst united electrons with holes via contact interface mediator, which retained the more negative conduction band (CB) potential and the more positive valence band (VB) potential, showing higher separation efficiency of photo-generated carriers and enhanced reduction and oxidation ability [29]. Silver halide (AgX, X = Cl, I, Br) was known for the photosensitive characteristic in photographic films [31]. AgX had also attracted concerns in photocatalytic field due to its great visible light response [32,33]. However, single AgX irregular particle spheres were inclined to agglomerate together thus causing unsatisfied photocatalytic performance [34]. It was anticipated to choose a suitable substrate to scatter AgX, restrain the aggregation and reduce the particle size strikingly. Therefore, it was reasonable to combine Bi_2WO_6 with AgBr to synthesize heterojunction, which simultaneously improved the photogenerated electron-hole pairs separation efficiency of Bi_2WO_6 and lowered the agglomeration of AgBr. Photocatalysts exhibited as thin film or suspended powders. Thin film photocatalysts featured for easy re-collection compared to powder photocatalysts [35]. However, the preparation of photocatalyst films first need to prepare the precursor solution and then deposited powder photocatalyst onto the solid substrates, which increased the preparation difficulty of catalyst [36,37]. To focus more on the synthesis method and still achieve the perfect photocatalytic activity, powder photocatalyst was fabricated.

Stimulated by the discussions above and the previous reports [38–40], a novel hierarchical flower-like Z-scheme AgBr/Bi_2WO_6 photocatalyst was successfully synthesized through the simplified hydrothermal and in-situ deposition–precipitation method, which expressed better control of flower-like morphology. The photocatalytic performance was creatively evaluated with the degradation of TC under visible light irradiation. The mineralization and degradation pathway of TC were explored with three-dimensional excitation-emission matrix fluorescence spectroscopy (3D EEMs) and liquid chromatography-mass spectrometry (LC-MS) methods. The recyclability experiment was performed by filtration. Moreover, the effects of initial TC concentration, coexistence ions, pH and light sources were also comprehensively studied. At last, the Z-scheme charge transfer mechanism with Ag nanoparticles (Ag NPs) as the electron mediator was validated by radicals trapping and electron spin resonance (ESR) experiments.

2. Experimental section

2.1. Materials

sodium tungstate dihydrate ($Na_2WO_4{\cdot}2H_2O$), Bismuth nitrate pentahydrate ($Bi(NO_3)_3{\cdot}5H_2O$), silver nitrate ($AgNO_3$), potassium bromide (KBr), 1, 4-benzoquinone (BQ), sodium oxalate ($Na_2C_2O_4$) and isopropanol (IPA) purchased from Chinese medicine group chemical reagent co., Ltd were all analytical reagents. Ultrapure water was gained from the Milli-Q ultrapure (18.25 MΩ cm) system in this experiment.

2.2. Synthesis of Bi_2WO_6 and AgBr/Bi_2WO_6 heterojunctions

Flower-like spherical Bi_2WO_6 was synthesized through a hydrothermal method. Typically, $Bi(NO_3)_3{\cdot}5H_2O$ (0.97 g) was ultrasonically dissolved in 60 mL of nitric acid solution (0.4 mol L^{-1}) for 6 min. 0.05 mol L^{-1} of Na_2WO_4 solution was added drop by drop into the above solution and magnetically stirred for 60 min at a speed of 500 r min^{-1}. Then the resulting suspension was poured into a 100 mL Teflon-lined autoclave which was sealed in a stainless steel tank and heated at 160 °C for 20 h. Subsequently, after naturally cooling to room temperature, the product (denoted as BWO) was washed and dried at 70°C for 10 h.

AgBr/Bi_2WO_6 heterojunctions were synthesized by a deposition–precipitation method. Briefly, Bi_2WO_6 (0.7 g) and Proportionate amounts of $AgNO_3$ were ultrasonically dissolved in 50 mL of deionized water then magnetically stirred for 30 min in the dark. Afterwards, the corresponding KBr solution was added dropwise with stirring in the dark for 60 min. Lastly, the yellow precipitate was washed then dried at 60 °C for 10 h. According to the amount of $AgNO_3$ (0.2, 0.4, 0.9, 2.5 mmol), samples of AgBr (5 wt%)/Bi_2WO_6, AgBr (10 wt%)/Bi_2WO_6, AgBr (20 wt%)/Bi_2WO_6 and AgBr (40 wt%)/Bi_2WO_6 were obtained (denoted as ABW-5, ABW-10, ABW-20 and ABW-40, respectively). Single AgBr was prepared through the same step in the absence of Bi_2WO_6. Fig. 1 displayed the schematic illustration of the synthetic processes of single BWO and ABW composites.

2.3. Characterization

The crystal structure of the sample was obtained by X-ray diffraction (XRD, Bruker D8 Advance instrument) in a 2θ range of 10–80°. The morphology was examined by field-emission scanning electron microscope (SEM, Hitachi S4800) and transmission electron microscopy (TEM, Tecnai G20). X-ray photoelectron spectroscopy (XPS) was performed (Thermo ESCALAB250XI spectrometer with monochromatic Al Kα radiation) to measure the surface elements and valence state of the prepared samples. UV–vis diffuse reflectance spectra (DRS, Hitachi U-4100) were measured with $BaSO_4$ as the reference. The Brunauer-Emmett-Teller (BET) specific surface area was analyzed on TRISTAR-3000 analyzer. Three-dimensional excitation-emission matrix fluorescence spectroscopy (3D EEMs) was performed on F-4500 spectrofluorimeter. Edinburgh FLsp920 transient fluorescence spectrometer was adopted for photoluminescence (PL) spectroscopy. The electron

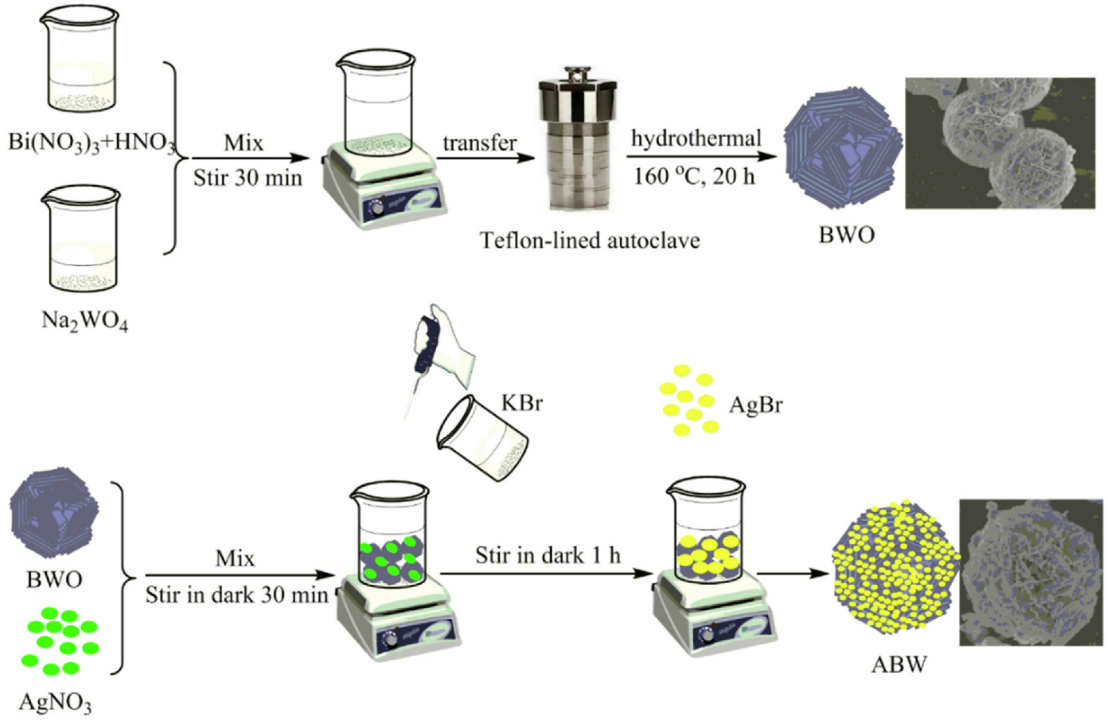

Fig. 1. Schematic illustration of the synthetic processes of single BWO and ABW composites.

spin resonance (ESR) measurements were performed on Bruker ER200-SRC spectrometer (visible light, $\lambda > 420$ nm). The Zeta potential of the material under different pH values was detected with Zeta-sizer Nano-ZS (Malvern). Electrochemical measurements were carried out via a CHI760E electrochemical workstation with a standard three-electrode system. The details were provided in the Supporting Information.

2.4. Photocatalytic degradation processes

TC was selected as the model pollutant to evaluate the photocatalytic performance of the prepared photocatalysts under visible light irradiation. The Xe lamp with 420 nm filter was used as the light source. Briefly, 50 mg of material was dispersed into TC solution (50 mL, 20 mol L^{-1}). Before illumination, the suspension was stirred in the dark for 30 min to reach the adsorption–desorption equilibrium. 4 mL of suspension was taken with a syringe every 10 min of visible light irradiation and passed through a 0.45 μm filter to obtain the supernatant liquid. A UV–vis spectrophotometer (Shimadzu UV-2450) was used to measure the concentration of TC (absorption wavelength: 357 nm). For a change, 4 mL of suspension was collected every 30 min to perform TOC analysis with Shimadzu total organic analyzer. Trapping experiments of active species were carried out by adding isopropanol (IPA, 50 mM), sodium oxalate ($Na_2C_2O_4$, 50 mM), and 1, 4-benzoquinone (BQ, 0.4 mM) to capture hydroxyl radicals (·OH), holes (h^+) and superoxide radicals (O_2^-), respectively. Photodegradation intermediates evaluation based on the LC-MS system and the solution toxicity during treatment assessment were supplied in the Supporting Information.

3. Results and discussions

3.1. Characterizations

XRD technique was adopted to analyze the compositions and crystal structures of the samples. Fig. 2 revealed the XRD patterns of single BWO, single AgBr, ABW-5, ABW-10, ABW-20 and ABW-40 composites. Characteristic peaks at 2θ values of 28.31°, 32.93°, 47.16° and 55.83° agreed well with (1 1 3), (0 2 0), (2 2 0) and (3 1 3) crystal planes of orthorhombic BWO (JCPDS NO. 73–1126) [27]. Characteristic peaks 2θ values of 26.73°, 30.96°, 44.35°, 55.04°, 64.48° and 73.26° could be related to (1 1 1), (2 0 0), (2 2 0), (2 2 2), (4 0 0) and (4 2 0) crystal planes of AgBr (JCPDS NO. 06-0438) [41]. The peaks of single BWO and single AgBr were unambiguous and there were no additional diffraction peaks, which reflected the fine crystallinity and high purity of the two samples. As depicted in Fig. 2, BWO modified with various ratios of AgBr included crystal phases of the two components. Among all the peaks existing in the composites, some peaks of AgBr gradually emerged and then boosted (crystal planes (2 2 0), (2 2 2), (4 0 0), (4 2 0)) or the peak existed all the time and its intensity enhanced (crystal planes (2 0 0)) with the increase of AgBr in the ABW composites, which exactly coincided with the variety of AgBr. The above analyses all proved that ABW composites were successfully obtained.

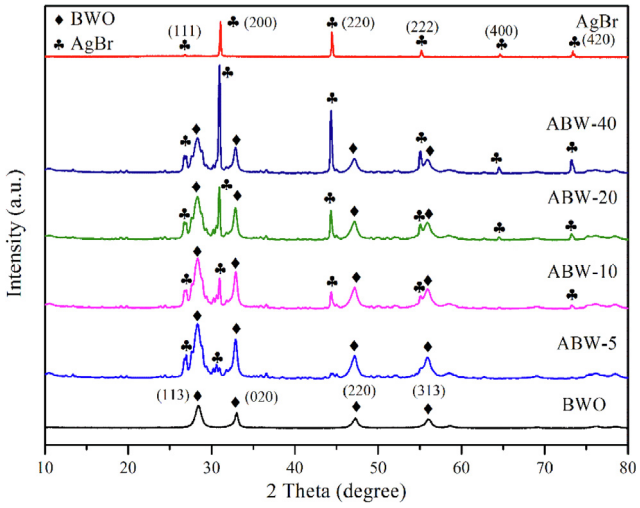

Fig. 2. XRD patterns of single BWO, single AgBr, ABW-5, ABW-10, ABW-20 and ABW-40 composites.

The elemental composition and chemical state of ABW-20

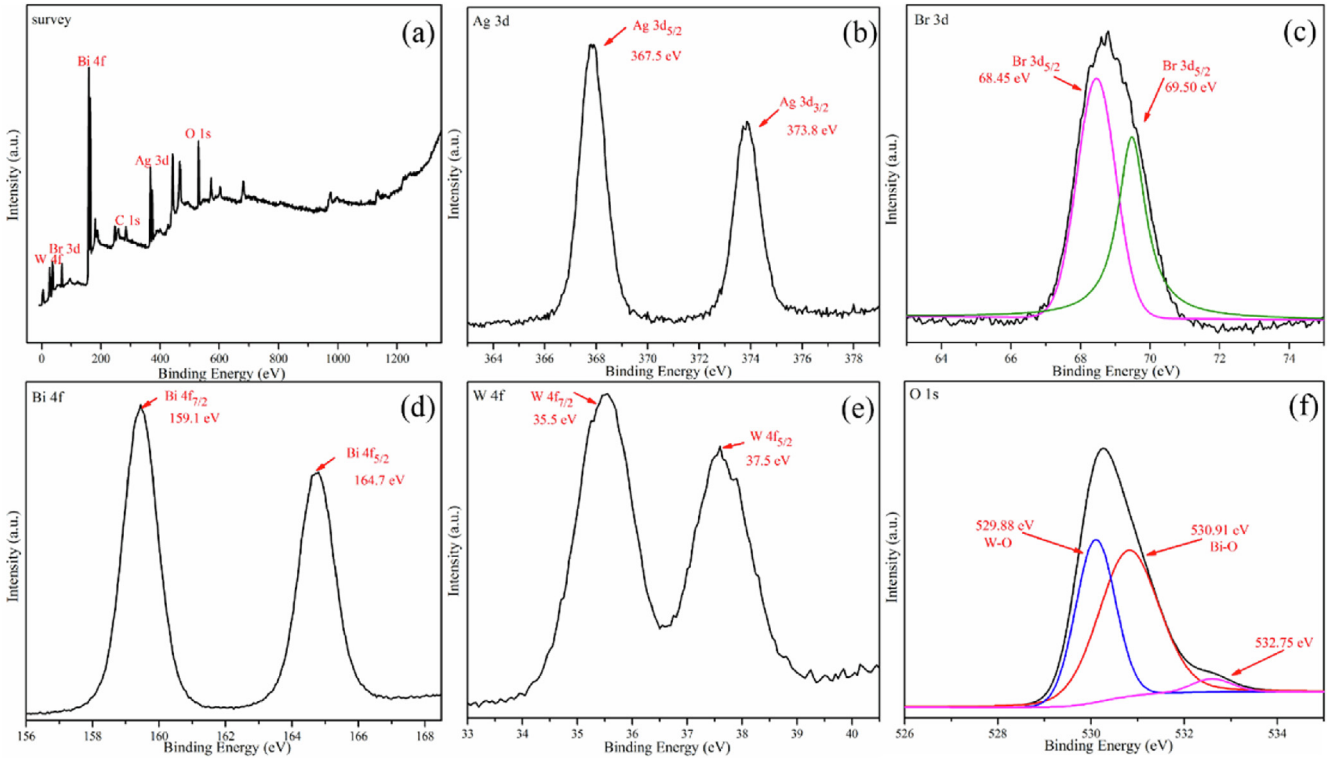

Fig. 3. XPS spectra of ABW-20 composite: (a) survey scan, (b) Ag 3d, (c) Br 3d, (d) Bi 4f, (e) W 4f, and (f) O 1 s.

composite were measured with XPS. Fig. 3a displayed the full survey spectrum of ABW-20, including elements of W, Bi, Br, C, Ag and O, among which peak for C derived from the adventitious hydrocarbon in the XPS instrument [42]. Peaks with binding energy of 367.99 eV and 374.07 eV were ascribed to Ag $3d_{5/2}$ and Ag $3d_{3/2}$ (Fig. 3b), which could not be further divided, implying that only Ag^+ emerged in the fabrication of the sample [43]. XPS of Br 3d locating at 68.45 eV and 69.50 eV (Fig. 3c) could be resolved to two peaks, which belonged to Br $3d_{5/2}$ and Br $3d_{3/2}$ of Br^-, respectively [41]. Peaks at 159.10 eV and 164.70 eV were in line with Bi $4f_{7/2}$ and Bi $4f_{5/2}$, respectively (Fig. 3d) [27]. One peak at 35.50 eV was indexed to W $4f_{7/2}$, and the other peak at 37.50 eV referred to W $4f_{5/2}$ (Fig. 3e) [27]. XPS of O 1 s could be deconvoluted into three peaks, indicating the complicated constituents of O element (Fig. 3f). Peaks at 529.88 eV and 530.91 eV were respectively assigned to the lattice oxygen of W-O bond ($[WO_4]^{2-}$) and Bi-O bond ($[Bi_2O_2]^{2+}$) [44]. Another peak at 532.75 eV represented the surface absorbed oxygen species [42]. In the light of the above evidences, ABW-20 was successfully obtained.

SEM technique was carried out to explore the morphology structures and particle sizes of single BWO, single AgBr and ABW-20 composite. As Fig. 4a revealed, single BWO displayed an about 4 μm-diameter flower-like spherical superstructure assembled by numerous nanoplates with smooth single crystal structure, thus forming interspace of varying sizes which increased the specific surface area in contact with pollutants. The amorphous BWO nanoparticles firstly self-aggregated then the two-dimensional nanoplate-like structure generated through “Ostwald ripening”. Finally, these nanoplates self-organized to flower-like BWO spherical superstructures [23]. The SEM image of AgBr (Fig. 4b) showed a series of spherical particles with diameters of 500 nm–1 μm. Compared to single AgBr, AgBr spherical particles loaded on the BWO flower-like sphere were transparently smaller (Fig. 4c). It was evident that AgBr nanoparticles examining about 5 nm were evenly loaded on the surface of porous spherical BWO, which made the surface of the composite rougher than single BWO. Therefore, depositing AgBr particles onto porous spherical BWO not only didn’t change the structure of BWO but also reduced the grain size of AgBr particles and further increased their dispersity. Typical TEM images also proved that AgBr nanoparticles were intimately anchored on the surface of BWO (Fig. 4g and h). HRTEM image of the fresh ABW-20 (Fig. 4i) affirmed the tight link between AgBr and BWO. The lattice *d*-spacings of BWO at 0.272 nm and 0.316 nm referred to (0 2 0) and (1 1 3) lattice planes, respectively [42]. Similarly, the lattice distance at 0.288 nm and 0.204 nm were attributed to (2 0 0) and (2 2 0) lattice planes of AgBr [41]. Accordingly, these results provided unimpugnable evidence that ABW heterostructure was achieved. Furthermore, energy dispersive X-ray spectroscopy (EDS) elemental mapping technique also validated the co-existence of Ag, Br, Bi, W and O elements (Fig. 5).

N_2 adsorption–desorption isotherm and the homologous Barrett-Joyner-Halenda (BJH) pore size distribution were employed to investigate the specific surface area and the pore characteristic of BWO and ABW-20 composite (Fig. 6). Table S1 disclosed the specific surface area, pore size and pore volume of BWO and ABW-20. The two samples manifested a type IV isotherm and a type H3 hysteresis loop, accompanied by the pore size distribution revealed the mesoporous structure [33]. The specific surface area of single BWO and ABW-20 were respectively 4.588 $m^2 \cdot g^{-1}$ and 8.286 $m^2 \cdot g^{-1}$, increased nearly by half. The smooth surface of BWO became rougher after loading AgBr, which indicated more available active sites for pollutants’ removal. However, the pore size of ABW-20 was lower than BWO, which could be ascribed to the filling of AgBr nanoparticles into BWO pores. Appropriate specific surface area and pore structure contributed to the high photocatalytic performance.

3.2. Photocatalytic performance analysis

The photocatalytic activity of the synthesized catalysts was firstly assessed through the degradation of TC under visible light illumination. Adsorption equilibrium for TC with catalysts was investigated in Fig. S1. Results showed that the adsorption for TC molecules increased rapidly in the first 10 min and then slowed down and the adsorption–desorption equilibrium was obtained in 30 min. The concentration of TC basically did not fluctuate in the blank experiment

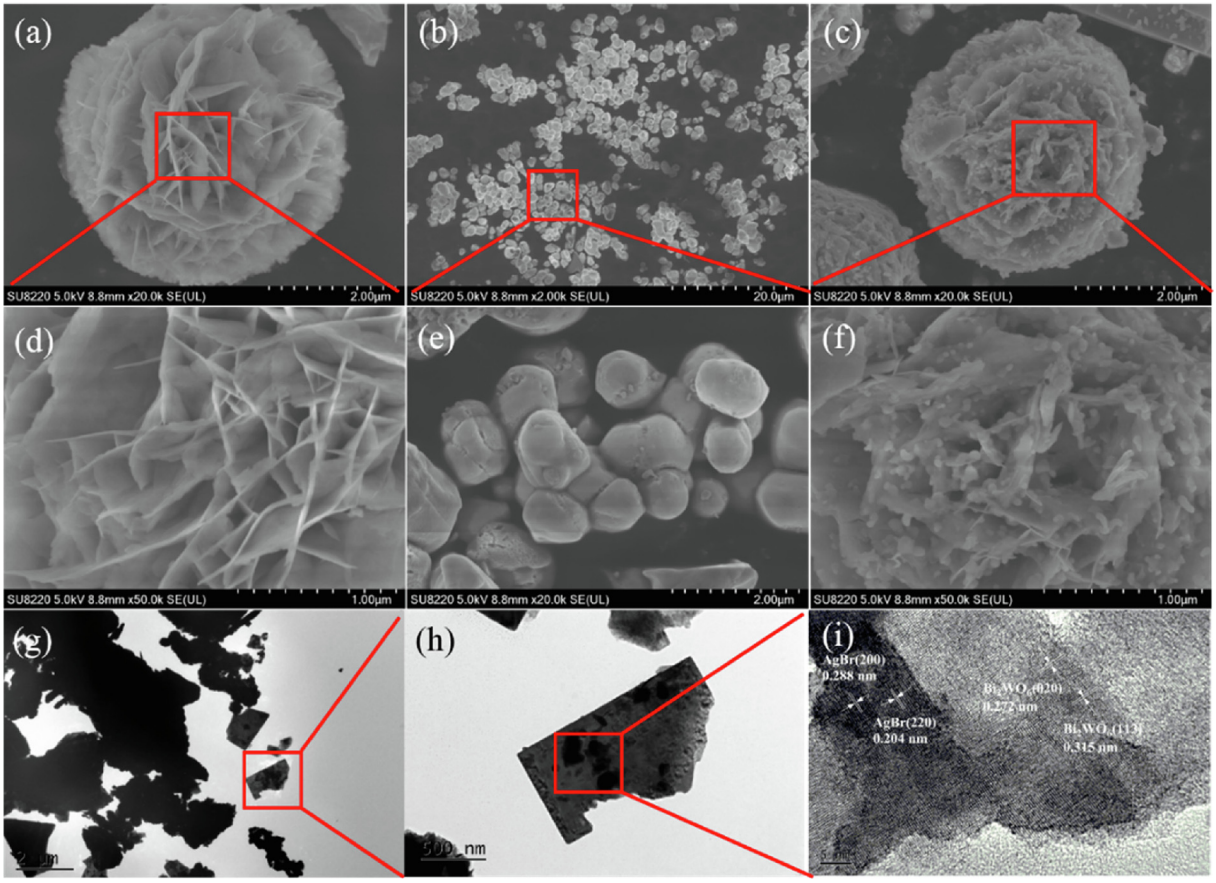

Fig. 4. SEM images of BWO (a and d), AgBr (b and e) and ABW-20 composite (c and f); TEM (g and h) and HRTEM (i) images of fresh ABW-20 composite.

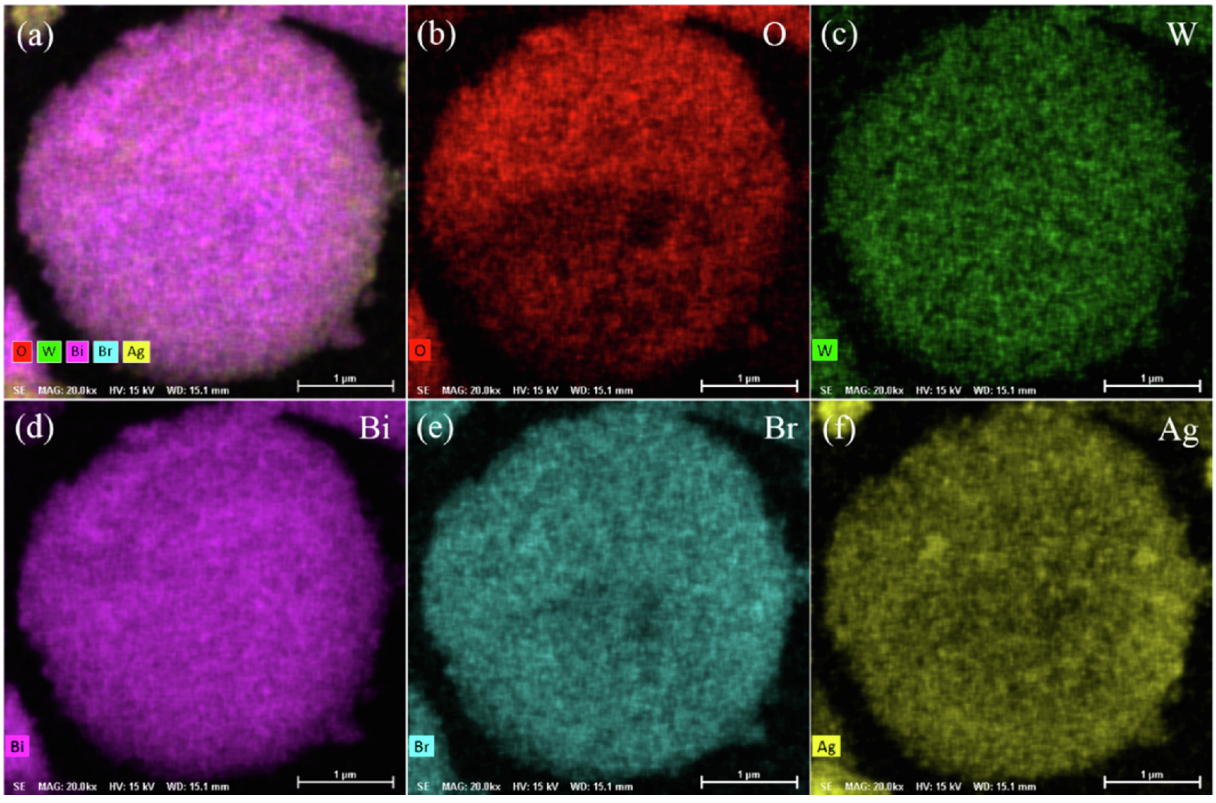

Fig. 5. SEM-EDS elemental mapping images of ABW-20 composite.

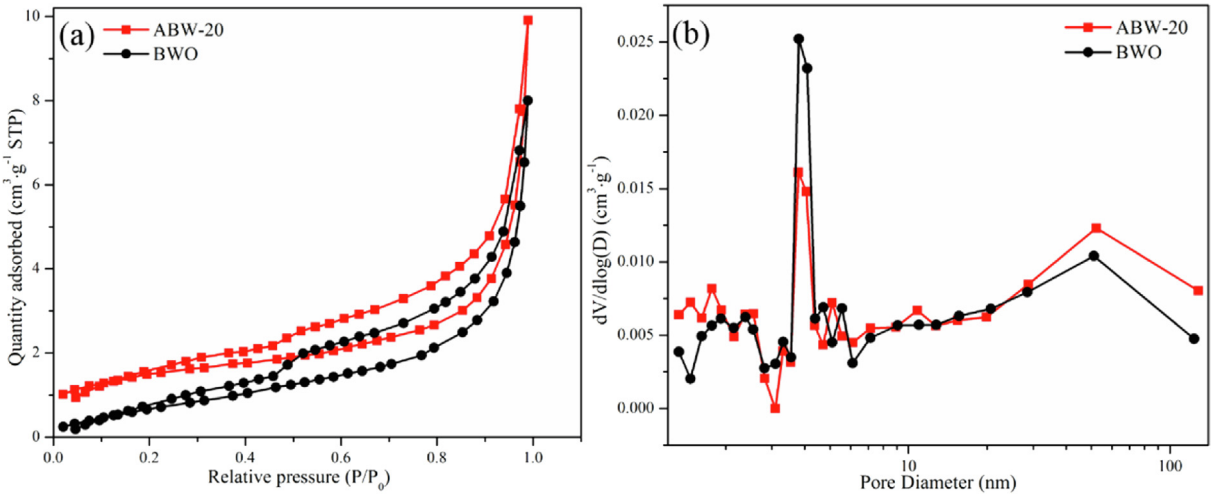

Fig. 6. N_2 adsorption–desorption isotherm (a) and the corresponding pore size distribution (b) of BWO and ABW-20 composite.

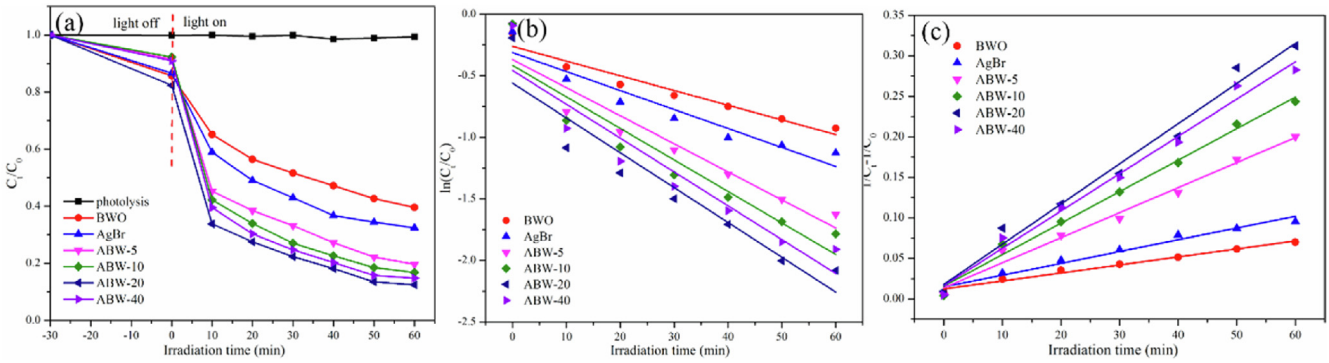

Fig. 7. (a) TC photocatalytic degradation curves; (b) pseudo-first-order kinetics curves and (c) pseudo-second-order kinetics curves of TC degradation.

excluding the self-degradation of TC (Fig. 7a). The removal efficiency of TC by BWO and AgBr under 60 min of visible light irradiation was 60.4% and 67.6%, respectively. Obviously, ABW composites exhibited superior photocatalytic performance compared to single BWO and AgBr. The enhanced photocatalytic performance of ABW composites could be assigned to the formation of heterojunction which advanced the insulation of photo-generated charges. With the amount of AgBr increasing to 20%, the highest degradation activity (87.5%) for TC was obtained. However, when AgBr exceeded 20%, the degradation efficiency declined. It was probably due to that excessive AgBr nanoparticles produced light shielding effect, which was unfavorable for the composites to absorb light [41]. The kinetics of TC photocatalytic degradation was investigated by the pseudo-first-order and pseudo-second-order models [45]:

$$-\ln(C_t/C_0) = k_1 t \quad (1)$$

$$1/C_t - 1/C_0 = k_2 t \quad (2)$$

where k_1 (min^{-1}) and k_2 (L·mg^{-1}·min^{-1}) were respectively the apparent rate constants of pseudo-first-order and pseudo-second-order kinetics. C_0 and C_t were pollutant concentrations at reaction time 0 and t min. The linear fitting of the two kinetics models were displayed in Fig. 7b and c and the corresponding apparent rate constants were listed in Table 1. The pseudo-second-order kinetic model conformed better to the photocatalytic degradation of TC based on the correlation coefficients (R^2). It was noteworthy that ABW-20 exhibited the largest apparent rate constant for TC, which was 5.02 times higher than BWO and 3.42 times higher than AgBr, indicating that there existed an optimal mass ratio of AgBr.

Table 1
Apparent rate constants of photocatalytic TC degradation from pseudo-first-order and pseudo-second-order models.

Samples	Pseudo-first-order kinetic		Pseudo-second-order kinetic	
	k_1 (min^{-1})	R^2	k_2 (L·mg^{-1}·min^{-1})	R^2
BWO	1.19×10^{-2}	0.93348	9.88×10^{-4}	0.98185
AgBr	1.54×10^{-2}	0.89530	1.45×10^{-3}	0.96763
ABW-5	2.28×10^{-2}	0.88855	3.09×10^{-3}	0.98140
ABW-10	2.56×10^{-2}	0.87312	3.89×10^{-3}	0.98961
ABW-20	2.82×10^{-2}	0.87521	4.96×10^{-3}	0.97891
ABW-40	2.75×10^{-2}	0.86889	4.60×10^{-3}	0.98484

3.2.1. *The effect of initial TC concentration*

TC concentration was a vital factor to the photodegradation efficiency and the practical application of the synthesized photocatalysts. With the concentration of TC increased from 20 mol L^{-1} to 60 mol L^{-1}, the degradation efficiency descended from 87.5% to 53.7% (Fig. 8a). The decline in photocatalytic performance with the increase of TC concentration could be explained by the following two reasons. Firstly, high concentration of TC increased the difficulty of light penetration, making it difficult for photons to reach and act on the catalyst, which evidently diminished the photocatalytic efficiency [46]; Secondly, the increase of TC concentration would inevitably lead to the increase of intermediate products, which brought about a competitive effect between TC molecules and the intermediates [47]. Therefore, it is necessary that high-concentrated sewage should be diluted before treatment in practical application.

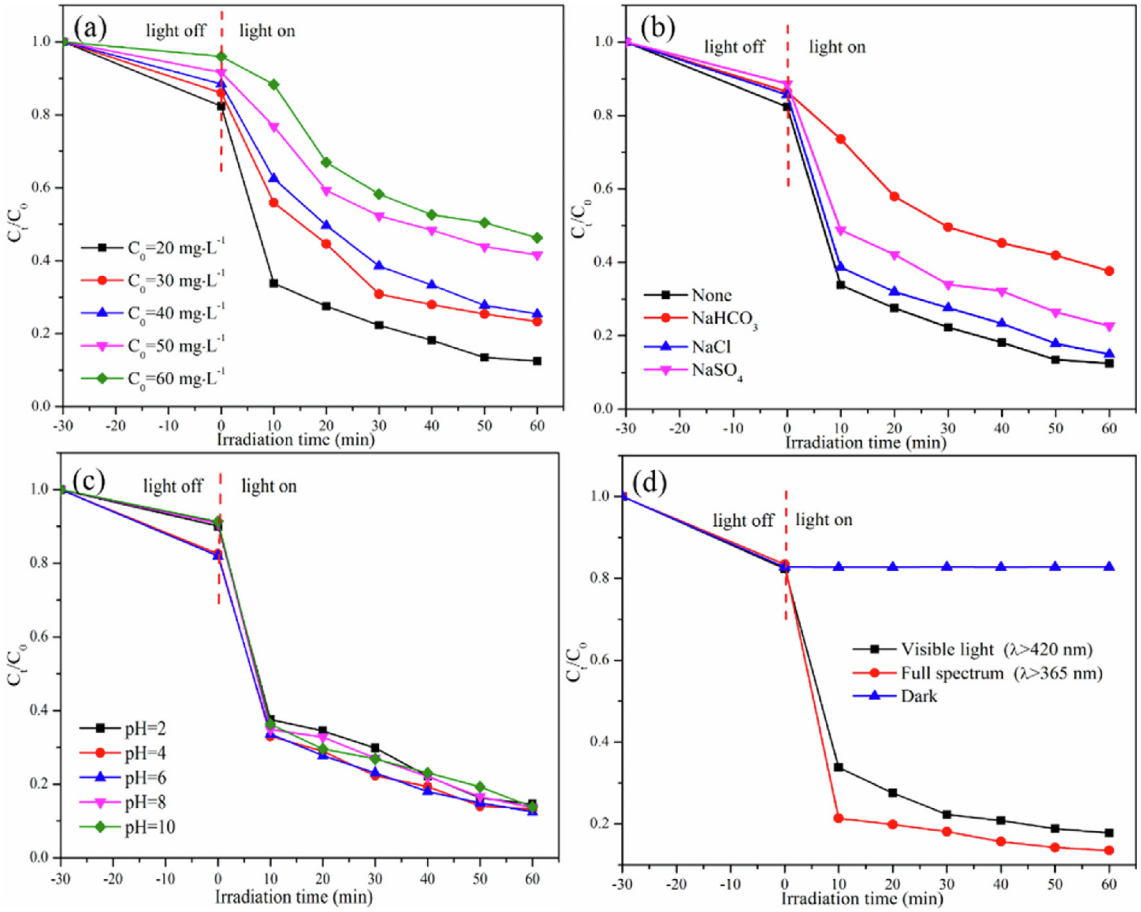

Fig. 8. The effects of (a) initial concentration, (b) coexistence ions, (c) reaction pH and (d) light sources for the photocatalytic degradation of TC in the presence of ABW-20.

3.2.2. The effect of coexistence ions

There existed multiple anions such as Cl^-, SO_4^{2-}, HCO_3^- in practical polluted water, which would interfere with the degradation of pollutants by photocatalysts. Hence, the effect of these ions on TC degradation should be investigated. As displayed in Fig. 8b (NaCl, Na_2SO_4 and $NaHCO_3$ as three model inorganic salts), the corresponding photodegradation efficiency sequence was NaCl > Na_2SO_4 > $NaHCO_3$. The slightest inhibitory effect was detected in the presence of NaCl, which might originate from the competitive adsorption effect between Cl^- and TC molecules, causing fewer active sites available [33]. The degradation of TC was strikingly hampered in the presence of Na_2SO_4 and $NaHCO_3$. SO_4^{2-} and HCO_3^- were effective radical scavengers for ·OH. Besides, HCO_3^- can also trap h^+ radicals. Therefore, the number of radicals participating in the photodegradation process was reduced, causing unsatisfied photocatalytic performance [46].

3.2.3. The effect of reaction pH

TC molecules were alert to pH owing to the protonation-deprotonation change. Therefore, the pH of TC solution was influential in the adsorption and photocatalytic capability. The initial pH of TC solution was adjusted by 1 M of HNO_3 or NaOH. TC which comprised carbonyl groups and tricarbonyl amide could form three species under different pH conditions [48]. When pH was under 3.3, TC molecules presented as cationic species (TCH^{3+}); When pH was 3.3–7.7, TC molecules appeared as zwitter ionic species (TCH_2^0); When pH was above 7.7, TC molecules emerged as anionic species (TCH^-/TC_2^-). The Zeta potentials of ABW-20 composite as a function of pH value was exhibited in Fig. S3. It was worth noticing that ABW-20 composite was positively charged when pH was under 6, and negatively charged when pH was over 6. When the initial pH of TC solution was at 2, 8 and 10, there were still considerable quantity of TC molecules absorbed onto the surface of ABW-20 composite despite the electrostatic repulsion between TC and ABW-20 (Fig. 8c). The TC adsorption was mildly enhanced under pH values of 4 and 6. It can be rationally concluded that it was not electrostatic interaction but surface complexation that played a decisive role in the adsorption capability of TC molecules [49]. In addition, the photocatalytic removal efficiencies hardly fluctuated regardless of the pH values, which signified that the pH value of TC solution didn't affect the photodegradation performance.

3.2.4. The effect of light sources

Solar light produced radiation of different energy, exerting an influence on the photocatalytic performance for pollutants removal. Fig. 8d displayed TC concentration change in the presence of ABW-20 when there is optical filter in front of the Xe lamp or in the dark condition. There was no striking decline of TC concentration in the dark except for the adsorption loss. In comparison to the procedure with the optical filter (λ > 420 nm), better degradation performance of ABW-20 for TC was achieved under full spectrum illumination (λ > 365 nm). It could be explained that shorter wavelength brought about the greater photon energy, accordingly resulting in the enhanced photocatalytic performance [47].

3.3. Optical absorption and charge transfer characteristics

Optical absorption properties of BWO, AgBr and ABW-20 were inspected with UV–vis DRS. As illustrated in Fig. 9a, ABW-20 manifested an enhanced visible light absorption and a red shift in absorption band

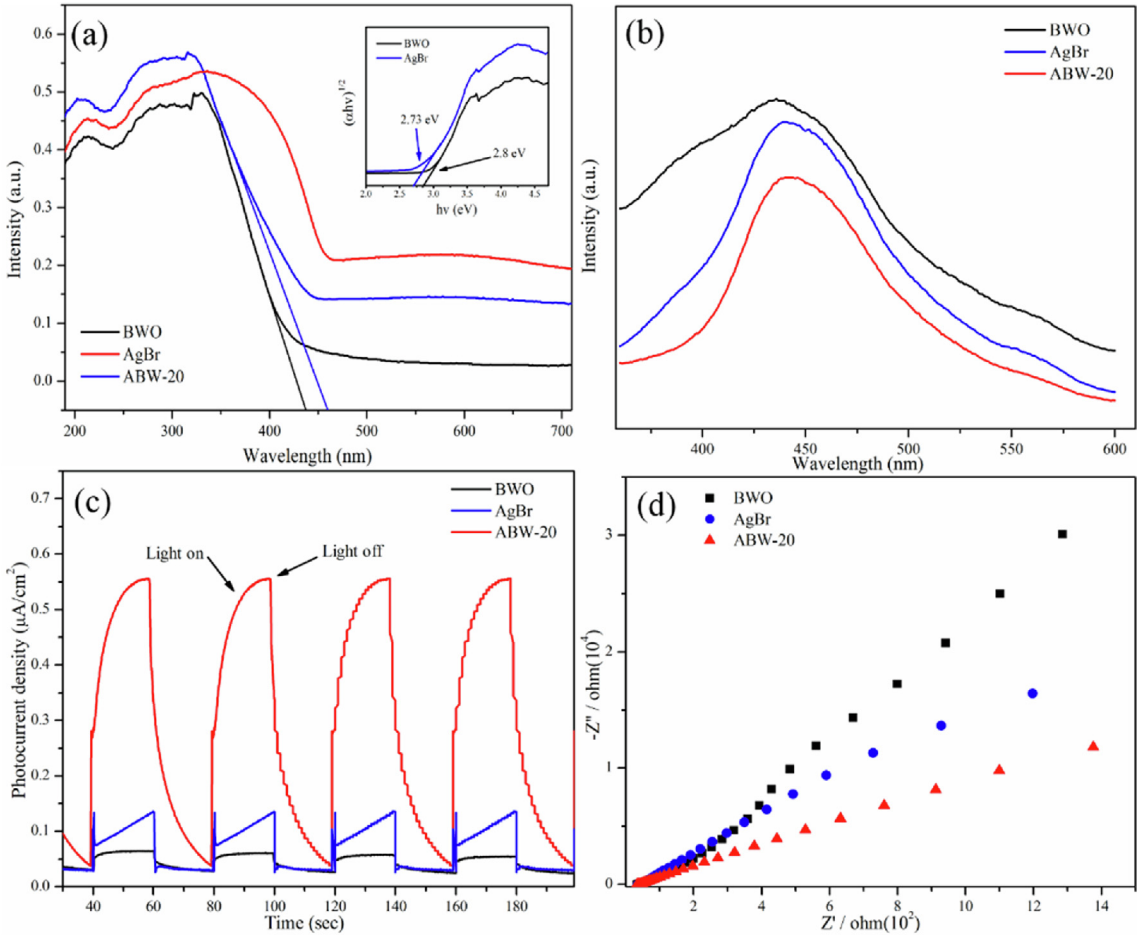

Fig. 9. (a) UV–vis DRS spectra (inset: the related bandgap); (b) PL spectra; (c) transient photocurrent response; (d) EIS Nyquist plots of BWO, AgBr and ABW-20.

compared with BWO and AgBr, whose absorption edges were at around 443 nm and 455 nm, respectively. The bandgap energy (E_g) of photocatalyst was depicted by the Kubelka–Munk function [50]:

$$\alpha h\gamma = A(h\gamma - E_g)^{\frac{n}{2}} \quad (3)$$

where *Eg, α, A, h,* γ represented energy gap, absorption coefficient, a constant, Planck's constant and light frequency, respectively. BWO and AgBr were all indirect transitions so 4 was selected as n value [51,52]. Detecting from the inset picture of Fig. 9a, the bandgaps of BWO and AgBr were about 2.8 eV and 2.73 eV, respectively.

Furthermore, the CB value (*ECB*) and VB value (*EVB*) of the semiconductor could be calculated by the equations below [21]:

$$E_{CB} = X - E^e - 0.5E_g \quad (4)$$

$$E_{VB} = E_{CB} + E_g \quad (5)$$

where *X* referred to the electronegativity of crystalline semiconductors, E^e was the energy of free electrons on the hydrogen scale (~4.50 eV vs NHE), *Eg* represented the energy gap of semiconductors. Therefore, the *ECB* values of BWO and AgBr were respectively 0.49 and −0.06 eV, and the corresponding *EVB* values of BWO and AgBr were 3.29 and 2.67 eV.

PL spectra was applied to explore the separation and recombination of photo-generated carriers of semiconductors [27]. Lower fluorescence intensity signified the lower recombination efficiency and the higher separation capacity of the photo-generated electron-hole pairs, which demonstrated the excellent photocatalytic performance. Fig. 9b displayed the PL spectra of BWO, AgBr and ABW-20 composite at an excitation wavelength of 325 nm. Apparently, compared with BWO and AgBr, ABW-20 composite presented a distinctly depressed PL intensity, implying that heterojunction between BWO and AgBr was favorable to suppress the recombination of photo-generated carriers and promote the separation of the electron-hole pairs.

Photo-generated electrons of the semiconductors could be motivated by visible light and transferred from the VB to CB to generate photocurrent. Herein, photocurrent tests were carried out to evaluate the migration and separation capability of the photo-generated carriers. Intuitively, all of the samples produced certain photocurrent responses. The photocurrent density remained at a low level under dark, but it swiftly increased when the light on and then dropped to the initial level under dark. BWO and AgBr showed a cliff-type decline while ABW-20 presented a sloped fall. As Fig. 9c illustrated, the transient photocurrent density of BWO, AgBr and ABW-20 composite were respectively 0.06, 0.13 and 0.56 μA cm^{-2}. ABW-20 expressed a ridiculously intensive photocurrent density, which was respectively 9.33 and 4.31 times higher than BWO and AgBr. The introduction of AgBr produced Ag NPs under visible light illumination, which functioned as the electron mediator to promote charge transfer during the photocatalytic process, resulting in the boosted photocurrent density. Consequently, the heterojunction between BWO and AgBr accelerated the migration of charge carriers and favored the degradation of organic pollutants.

The charge transfer capability was measured by electrochemical impedance spectroscopy (EIS) Nyquist. The smaller the arc radius was, the smaller the charge transfer resistance was, thus leading to a more efficient separation of carriers [31]. ABW-20 composite obviously reflected the smallest arc radius, indicating the highest charge separation efficiency (Fig. 9d). The results above were in good consistency with the photocatalytic degradation performance.

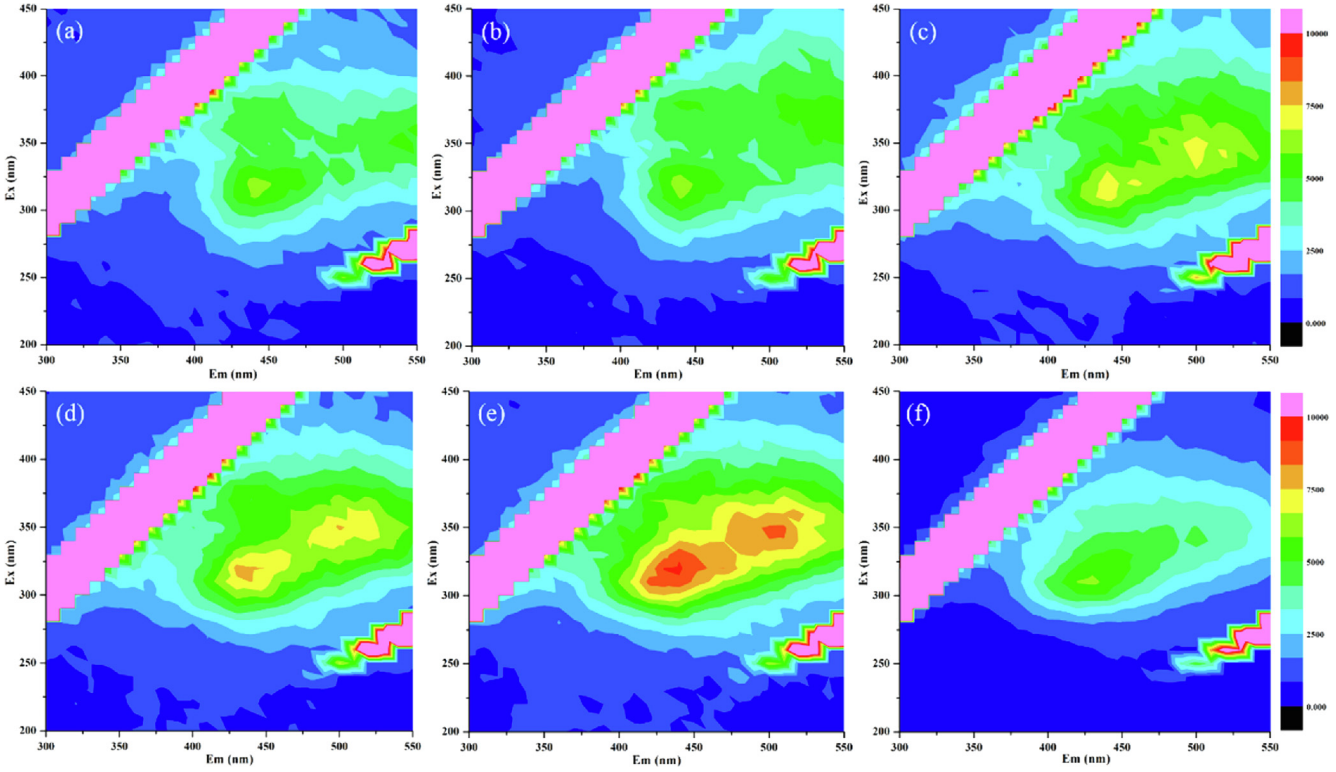

Fig. 10. 3D EEMs results of TC photodegradation: samples obtained (a) from the original solution; (b) after 30 min dark reaction; and (c-f) with visible light irradiation time of 10 min, 30 min, 60 min and 120 min, respectively.

3.4. 3D EEMs analysis and TOC measurement of TC

3D EMMs were utilized to investigate the degradation behavior and mineralization degree of TC during the photocatalytic process (Fig. 10). Fluorescence characteristic was closely related to the structure and functional groups in molecules [53]. The available literature proved that TC molecular produced characteristic fluorescence signals during the degradation process [43,54]. It was obvious that the fluorescence spectra basically remained unchanged before illumination, which implied that adsorption did not alter TC molecular structure. Peaks at Ex/Em of 300–340/410–475 nm and Ex/Em of 325–370/475–555 nm representing humic acid-like organics began to appear and the fluorescence intensity strengthened over time (from 10 min to 60 min) [55]. When the reaction time extended to 120 min, the two characteristic peaks vanished, demonstrating that the humic acid-like organics generated in the photodegradation process further mineralized to intermediates with lower molecular weight.

TC mineralization with BWO and ABW-20 were also detected by TOC measurement. The TOC removal efficiency was calculated with following formula:

$$TOC removal efficiency(\%) = (TOC_0 - TOC_t)/TOC_0 \quad (6)$$

where TOC_0 referred to the initial TOC, TOC_t represented different TOC at selected time. TOC removal efficiency of BWO was always lower than that of ABW-20 as perceived in Fig. 11. The mineralization efficiency ascended with the prolonging time, implying that the mineralization process advanced constantly. After 90 min degradation, about 39.4% TC was mineralized by ABW-20, which was much lower than the degradation efficiency. It could be rationally concluded to the intermediate products that could retard the mineralization [56].

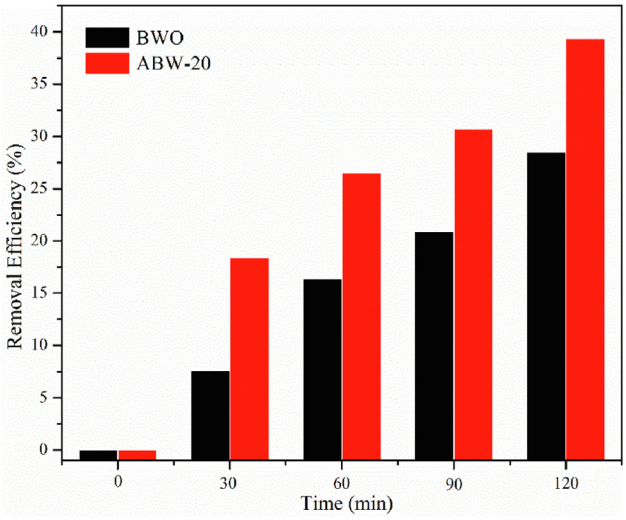

Fig. 11. The total organic carbon (TOC) removal efficiencies of BWO and ABW-20.

3.5. Possible degradation pathway of TC

LC-MS was applied to identify the degradation intermediates of TC with ABW-20 composite in detail. MS spectra of TC and possible intermediates at different reaction time were presented in Fig. S4. *m/z* of 445.2 was deemed to TC peak, whose intensity gradually weakened with the proceeding of the degradation, indicating the destruction of TC. Peaks of intermediates began to appear at 30 min irradiation time (Fig. S4b). Intensity of some intermediates with *m/z* of 284, 431, 461 and 475.3 attenuated, demonstrating that these intermediates were further degraded. Moreover, when the illumination time extended to 90 min, some new intermediates such as *m/z* of 342, 359.2, 398.1 and 416 emerged and intermediate with *m/z* of 405.2 vanished (Fig. S4c), which depicted the further degradation process of TC. Fig. 12 raised three proposed photocatalytic degradation pathways of TC with ABW-

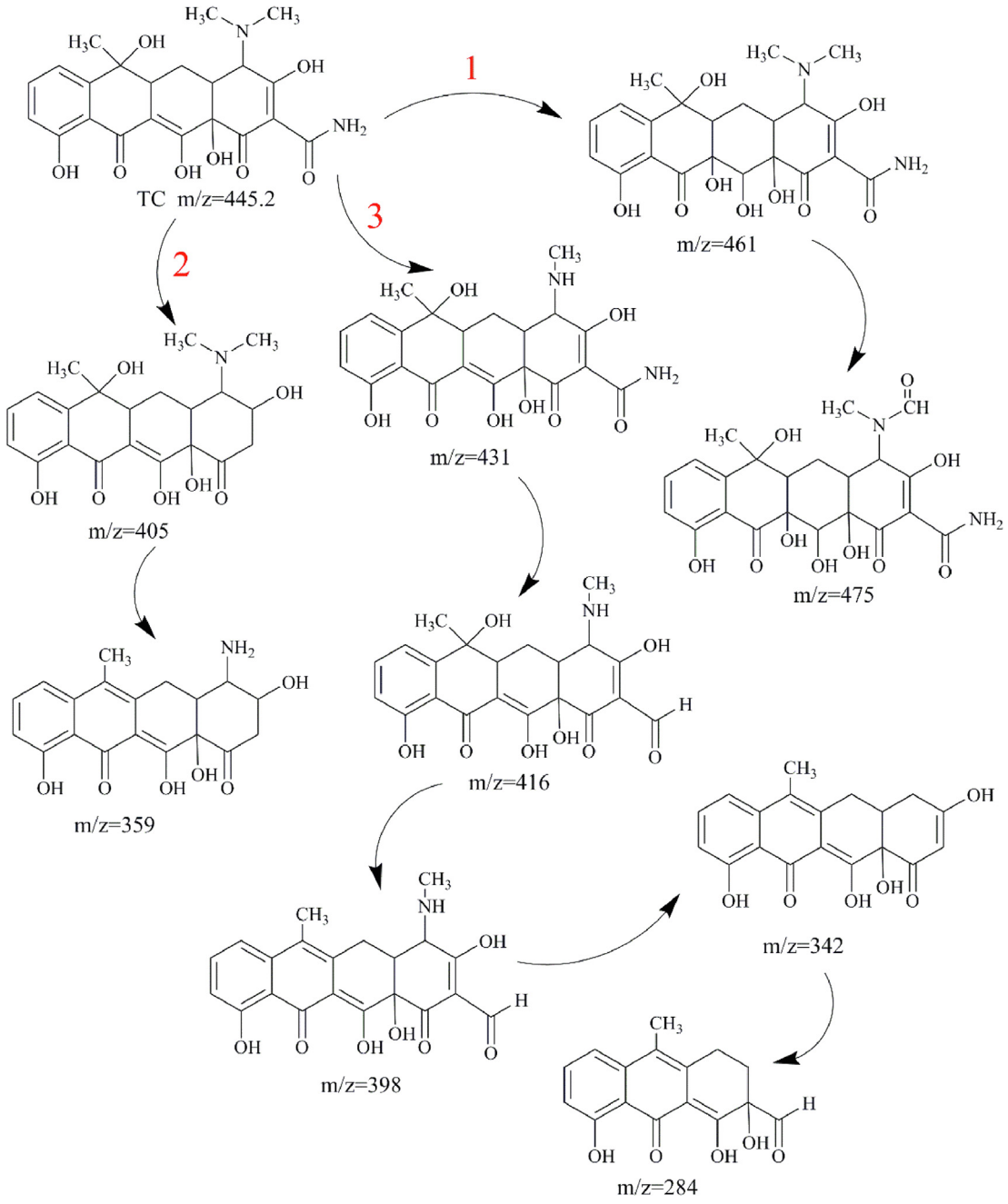

Fig. 12. Proposed photocatalytic degradation pathways of TC with ABW-20.

20. Pathway 1: hydroxylation process (m/s 461, m/s 475) [33]. Pathway 2: deamidation reaction (m/s 405) and loss of dimethylamino group (m/s 359) [57]. Pathway 3: TC molecule was destroyed through a series of loss of N-methyl group (m/s 431), amino group (m/s 416) and H_2O molecule (m/s 398), aldehyde group (m/s 342) and opening of benzene rings (m/s 284) [58]. Ultimately, these cyclic intermediates could transform to short-chain carboxylic acids [59,60].

Besides, the toxicity of reaction solution during treatment was also evaluated with traditional bacterial growth (gram-negative strain E. *coli*). Generally speaking, the higher degree of mineralization favored the reduction of toxicity to bacteria [61]. As displayed in Fig. S5, the inhibition rate of original TC solution (0 min) was about 30.4% and the inhibition rate of reaction solution raised with the prolonging of the irradiation time, which indicated that the intermediate products of TC photocatalysis would trigger the toxicity enhancement towards bacteria. The similar phenomenon had been observed by the former researches [62,63]. It was probably due to that TC molecules degraded to some other products that were more deleterious than the parent molecules instead of the complete mineralization. The result coincided with the TOC measurement, demonstrating that the treated TC solution should be processed properly in practical application.

3.6. Photostability and recyclability of ABW-20 composite

Practical applications required advantageous recyclability of photocatalytic materials for the aim of cutting cost and refraining from secondary pollution. TC degradation experiment was carried out for four times in a row. As disclosed in Fig. 13, degradation efficiency of TC didn't descend distinctly after four cycles under the identical condition (only 5.8% loss). Retaining a high performance signified the excellent photostability of ABW-20 composite.

Additionally, the cycled ABW-20 composite was characterized by

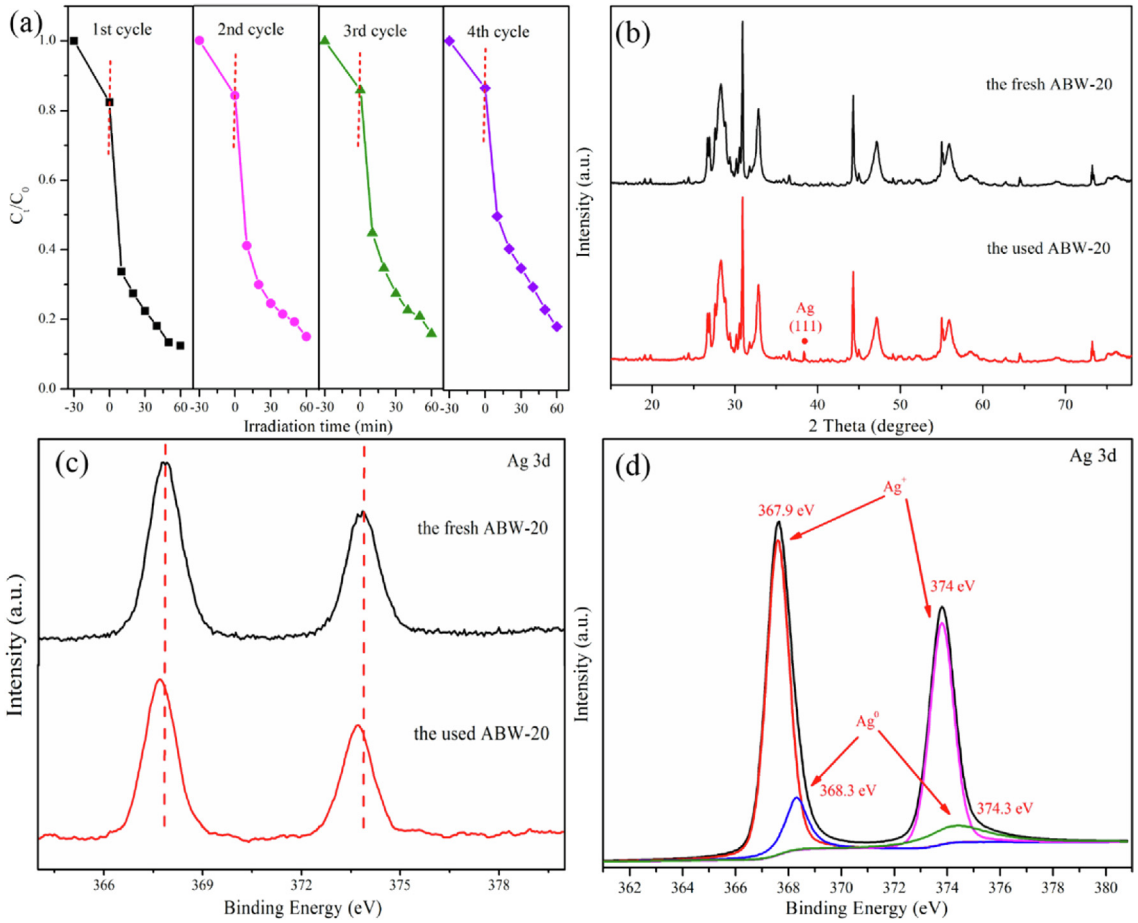

Fig. 13. (a) Cycling test of TC photocatalytic degradation with ABW-20; (b) XRD patterns comparison of the fresh and used ABW-20; (c) Ag XPS spectrum comparison of the fresh and used ABW-20; (d) Ag high resolution XPS spectrum of the used ABW-20.

XRD, XPS and HRTEM for more composition and structural information to further certify the photostability of ABW-20 composite. Fig. 13b displayed the XRD patterns of the used ABW-20 composite, which was almost the same as the fresh one. However, there existed a special weak peak at 38.38°, representing the (1 1 1) crystal plane (JCPDS card NO. 65–2871) of Ag NPs [43], which was clearly observed in the amplified partial XRD patterns (Fig. S6). Comparing the Ag XPS spectra of the fresh composite with the used one (Fig. 13c), a mild shifting was found in the XPS peaks, which could be ascribed to the emergence of elemental Ag. Besides, XPS peak of the used ABW-20 composite were divided into four peaks (Fig. 13d). Peaks with binding energy of 367.9 and 374 eV were for Ag^+ $3d_{5/2}$ and Ag^+ $3d_{3/2}$ and energy of 368.3 and 374.3 eV were for Ag^0 $3d_{5/2}$ and Ag^0 $3d_{3/2}$, respectively [43]. The relative amount of metallic Ag to Ag^+ in the used ABW-20 composite was determined to be 20.14% [64], which also verified the existence of Ag. Moreover, Fig. S7 supplied the TEM and HRTEM images of the used ABW-20 composite. The *d*-spacing reckoned to be 0.236 nm was lattice plane of metallic Ag (1 1 1) [43]. Based on all the proofs above, ABW-20 composite maintained high stability after use and the heterojunction between BWO and AgBr took effect constantly. In addition, Ag NPs served as electron mediator to advance the shift and separation of photo-generated carriers, which could be validated in next chapter. Accordingly, the excellent stability of ABW-20 composite made it possible to be applied in the environmental remediation.

3.7. Mechanisms of enhanced photocatalytic performance

Radicals trapping experiments should be implemented because active radicals produced in the process of photocatalysis played an important role in TC degradation process. Fig. 14a and b displayed the inhibitory effect of different scavengers for ABW-20 composite. The TC removal rate was slightly suppressed by adding $Na_2C_2O_4$ quencher, indicating that h^+ played a tiny part in the degradation process. When isopropanol was added, TC degradation efficiency decreased from 87.5% to 72.9%, demonstrating that ·OH played a more essential role. Comparatively, $\cdot O_2^-$ exerted the biggest influence on TC degradation with the efficiency dropped by more than half (from 87.5% to 41.5%) adding 1.4-benzoquinone. Therefore, ·OH, h^+ and $\cdot O_2^-$ produced effect on TC degradation in varying degrees. Additionally, radicals trapping experiments were also carried out with BWO, and the results (Fig. S8a and b) showed that ·OH and $\cdot O_2^-$ strikingly affected the TC degradation, while h^+ did not work evidently.

The ESR techniques were performed to further identify the generation of $\cdot O^{2-}$ and ·OH in ABW-20 composite under visible light. As perceived in Fig. 14c, four notable signals which were ascribed to DMPO-O^{2-} were detected under 5 min visible light irradiation with ABW-20 composite and the peak intensities boosted under 10 min illumination. While there was no signal in the dark. It could be concluded that O_2 was reduced to $\cdot O_2^-$ under visible light irradiation. Similar phenomenon also applied to DMPO-OH for ABW-20 composite, indicating that ·OH emerged. Both radicals trapping and ESR experiments validated the major role of ABW-20 composite played in photocatalytic degradation. For BWO (Fig. S8c and d), DMPO-O^{2-} and DMPO-·OH signals were captured under visible light but no signal in the dark, which was consistent with the radicals trapping results. Noticeably, signal intensity for single BWO under visible light was not so high as ABW-20, demonstrating that ABW-20 exhibited a superior photocatalytic performance.

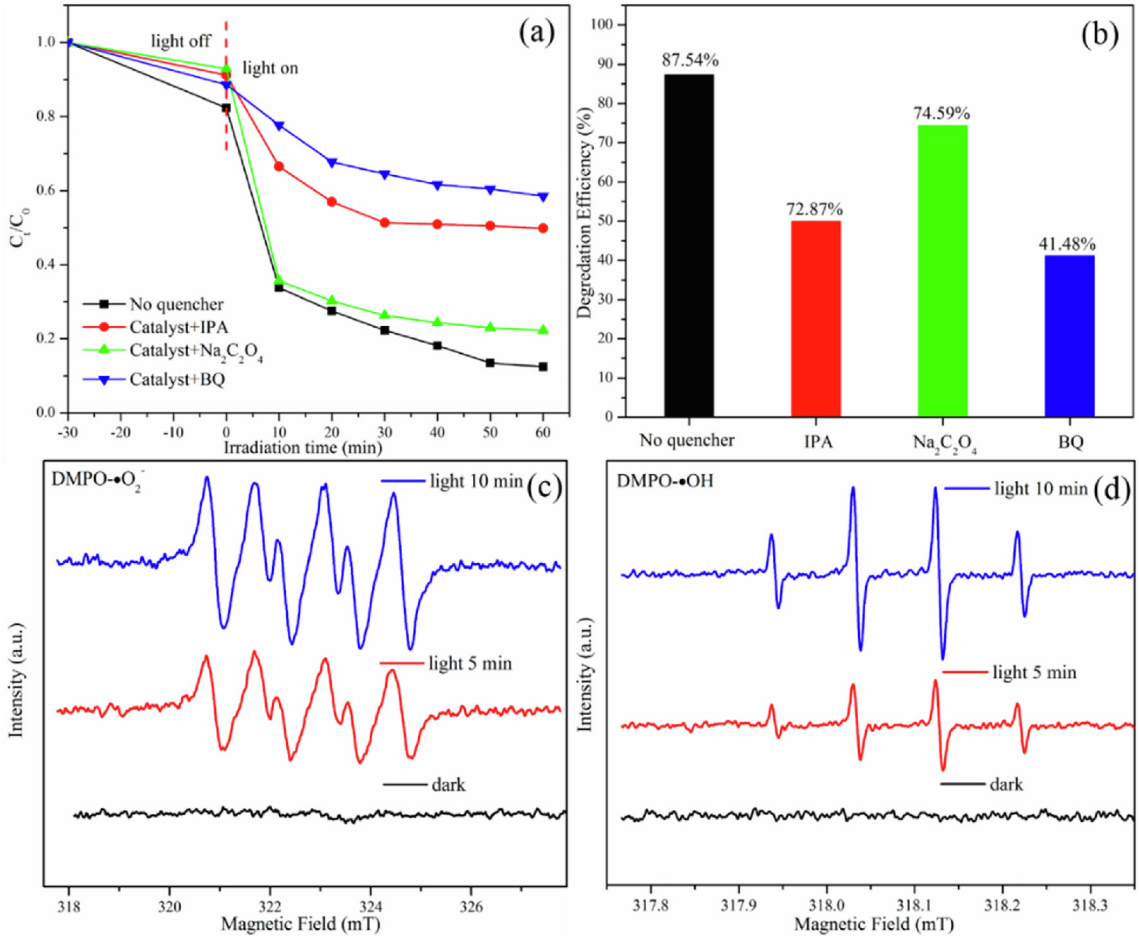

Fig. 14. Trapping experiments of decomposing TC by adding different scavengers with ABW-20 composite (a and b); ESR spectra by adding DMPO to capture $\cdot O^{2-}$ and ·OH with ABW-20 composite (c and d).

Based on the UV–vis DRS spectra and Eqs. (4) and (5), the E_{CB} and E_{VB} of BWO were 0.49 and 3.29 eV, with the homologous E_{CB} and E_{VB} of AgBr being −0.06 and 2.67 eV, respectively. Accordingly, a conventional heterojunction model was raised in the light of the band position of BWO and AgBr (Fig. 15a). The two semiconductors were excited to produce photo-generated electrons (e^-) and holes (h^+) with electrons transferring from CB of AgBr to the CB of BWO and holes migrating from VB of BWO to the VB of AgBr under visible light irradiation. However, electrons in the CB of BWO could not reduce O_2 into $\cdot O_2^-$, resulting from the more positive CB potential of BWO (0.49 eV vs. NHE) than $O_2/\cdot O_2^-$ potential (−0.046 eV vs. NHE) [41]. Similarly, holes in the VB of AgBr could not oxidize H_2O into ·OH because the VB potential of AgBr (2.67 eV vs. NHE) was more negative than $H_2O/\cdot OH$ potential ($H_2O/\cdot OH$: 2.72 eV vs. NHE) [41]. In that case, $\cdot O_2^-$ and ·OH were unable to produce in the degradation process and only h^+ reacted with TC, which contradicted the results of the radicals trapping tests and ESR results. That is to say, the conventional charge transfer model was impractical in ABW heterojunction. Consequently, the Z-scheme heterojunction system with Ag NPs as the electron mediator was depicted in Fig. 15b. AgBr was reduced to Ag NPs attached to the surface of ABW composites illuminated by visible light, converting AgBr/Bi_2WO_6 to Ag@AgBr/Bi_2WO_6. The emergence of Ag NPs was already certified by XRD, XPS and HRTEM based on the former analyses. According to the former literature, Ag NPs played two roles in Z-scheme heterojunction system: electron mediator and photosensitizer. The role Ag NPs played in the system was up to the two semiconductors' response to the incident light [29]. When one of or both of the two semiconductors cannot be excited by the incident light, Ag NPs served as the photosensitizer. When both the two semiconductors can absorb the photons from incident light, Ag NPs mainly acted as the electron mediator. In this research, Ag NPs served as electron mediator because both AgBr and BWO could be excited by visible light. Electrons moved from BWO (CB) to Ag NPs due to the higher CB potential of BWO than the Fermi level of Ag NPs [65]. While holes in AgBr (VB) migrated to Ag NPs as a result of the more positive VB potential of AgBr than the Fermi level of Ag NPs. Electrons and holes flowing into Ag NPs recombined swiftly, resulting in a quick charge transfer rate. Ag NPs fulfilled the spatial insulation of the photo-generated pairs, which extremely confined the undesirable recombination. The photo-generated electrons retained in the more negative CB of AgBr and holes retained in the more positive VB of BWO, resulting in the stronger redox ability. Electrons accumulating in the CB of AgBr easily reacted with O_2 to form $\cdot O_2^-$ and holes enriching in the VB of BWO also oxidized H_2O into ·OH promptly. Herein, h^+, $\cdot O_2^-$ and ·OH produced effect simultaneously in the degradation process. In brief, Z-scheme heterojunction carriers transformation system with ABW composites conformed perfectly to the excellent the photocatalytic performance.

$$Bi_2WO_6 + h\gamma \rightarrow e_{CB}^-(Bi_2WO_6) + h_{VB}^+(Bi_2WO_6) \quad (7)$$

$$AgBr + h\gamma \rightarrow e_{CB}^-(AgBr) + h_{VB}^+(AgBr) \quad (8)$$

$$e_{CB}^-(Bi_2WO_6) + Ag \rightarrow Bi_2WO_6 + e_{CB}^-(Ag) \quad (9)$$

$$h_{VB}^+(AgBr) + Ag \rightarrow AgBr + h_{VB}^+(Ag) \quad (10)$$

$$e_{CB}^-(Ag) + h_{VB}^+(Ag) \rightarrow recombination \quad (11)$$

$$h_{VB}^+(Bi_2WO_6) + H_2O \rightarrow \bullet OH(Bi_2WO_6) + H^+ \quad (12)$$

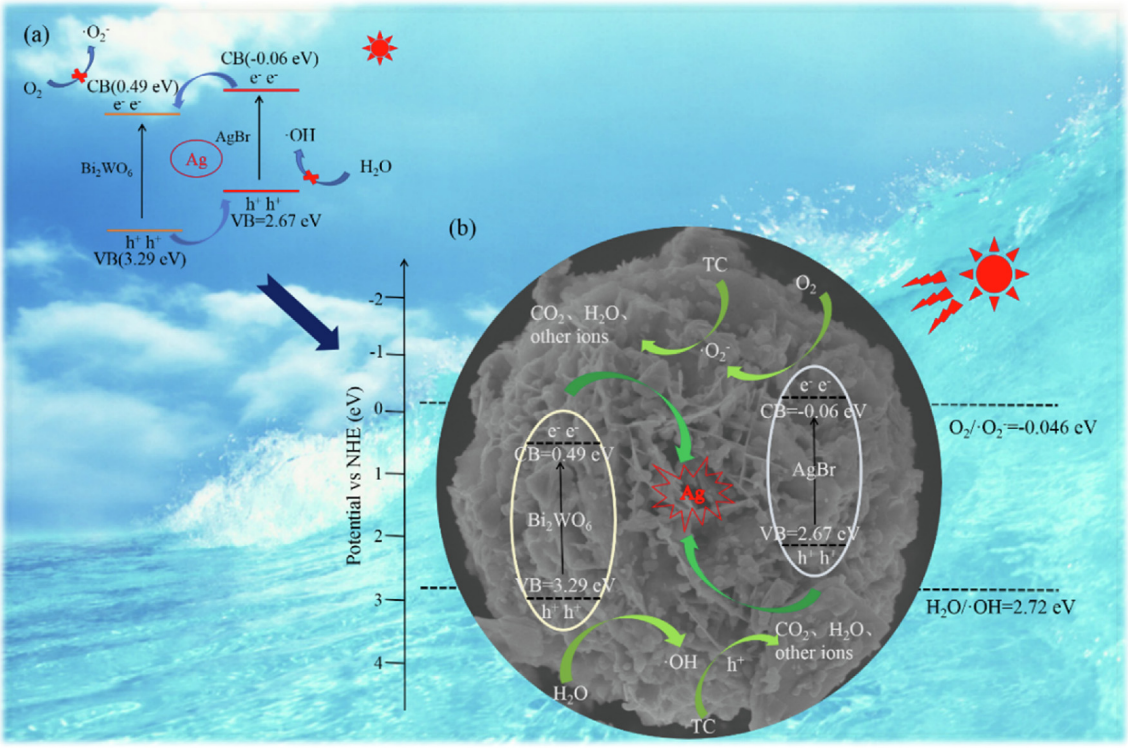

Fig. 15. Schematic illustration of the proposed reaction mechanism for TC degradation under visible light irradiation based on the conventional heterojunction (a) the Z-scheme heterojunction (b).

$$e_{CB}^{-}(AgBr) + O_2 \rightarrow \bullet O_2^{-}(AgBr) \quad (13)$$

$$\bullet OH\,(Bi_2WO_6)/\bullet O_2^{-}(AgBr)/h_{VB}^{+}(Bi_2WO_6) + TC \rightarrow products \quad (14)$$

4. Conclusions

All in all, the original ABW heterojunctions were favorably prepared via a multiple step: hydrothermal method was employed to synthesize flower-like spherical Bi_2WO_6 and in-situ deposition–precipitation procedure next deposited AgBr onto Bi_2WO_6. The prepared ABW heterojunctions produced Ag NPs during the photocatalysis process, thus converting AgBr/Bi_2WO_6 to Ag@AgBr/Bi_2WO_6. Consequently, a Z-scheme charge transfer mechanism featuring Ag NPs electron mediator was proposed, which realized 87.5% of photocatalytic efficiency for TC. In addition, Exploration of 3D EEMs and TOC jointly verified the mineralization of TC. LC-MS analysis further investigated the degradation pathway of TC: hydroxylation process, deamidation reaction and the loss of N-methyl group. Radicals trapping and ESR experiments validated the notable part h^+, $\cdot O_2^-$ and ·OH played for TC removal in the photocatalytic treatment. This strategy projected the unneglectable role Ag NPs played in the photocatalytic process, opened up a new road to efficient Z-Scheme heterojunction design and shed light on the preliminary understanding of the degradation pathway for TC.

Acknowledgements

This study was financially supported by the Program for the National Natural Science Foundation of China (51879101, 51579098, 51779090, 51709101, 51521006, 51809090, 51278176, 51378190), the National Program for Support of Top-Notch Young Professionals of China (2014), the Program for Changjiang Scholars and Innovative Research Team in University (IRT-13R17), and Hunan Provincial Science and Technology Plan Project (2018SK20410, 2017SK2243, 2016RS3026), and the Fundamental Research Funds for the Central Universities (531119200086, 531118010114, 531107050978).

Appendix A. Supplementary data

Supplementary data to this article can be found online at https://doi.org/10.1016/j.cej.2019.121991.

References

[1] D. Huang, X. Qin, Z. Peng, Y. Liu, X. Gong, G. Zeng, C. Huang, M. Cheng, W. Xue, X. Wang, Z. Hu, Nanoscale zero-valent iron assisted phytoremediation of Pb in sediment: Impacts on metal accumulation and antioxidative system of Lolium perenne, Ecotox. Environ. Safe. 153 (2018) 229–237.
[2] W. Xue, Z. Peng, D. Huang, G. Zeng, J. Wan, R. Xu, M. Cheng, C. Zhang, D. Jiang, Z. Hu, Nanoremediation of cadmium contaminated river sediments: Microbial response and organic carbon changes, J. Hazard. Mater. 359 (2018) 290–299.
[3] W. Xue, D. Huang, G. Zeng, J. Wan, M. Cheng, C. Zhang, C. Hu, J. Li, Performance and toxicity assessment of nanoscale zero valent iron particles in the remediation of contaminated soil: a review, Chemosphere 210 (2018) 1145–1156.
[4] D. Huang, C. Hu, G. Zeng, M. Cheng, P. Xu, X. Gong, R. Wang, W. Xue, Combination of Fenton processes and biotreatment for wastewater treatment and soil remediation, Sci. Total Environ. 574 (2017) 1599–1610.
[5] R. Wang, D. Huang, Y. Liu, Z. Peng, G. Zeng, C. Lai, P. Xu, C. Huang, C. Zhang, X. Gong, Selective removal of BPA from aqueous solution using molecularly imprinted polymers based on magnetic graphene oxide, RSC Adv. 6 (2016) 106201–106210.
[6] D. Huang, X. Wang, C. Zhang, G. Zeng, Z. Peng, J. Zhou, M. Cheng, R. Wang, Z. Hu, X. Qin, Sorptive removal of ionizable antibiotic sulfamethazine from aqueous solution by graphene oxide-coated biochar nanocomposites: influencing factors and mechanism, Chemosphere 186 (2017) 414–421.
[7] D. Huang, L. Liu, G. Zeng, P. Xu, C. Huang, L. Deng, R. Wang, J. Wan, The effects of rice straw biochar on indigenous microbial community and enzymes activity in heavy metal-contaminated sediment, Chemosphere 174 (2017) 545–553.
[8] X. Guo, Z. Peng, D. Huang, P. Xu, G. Zeng, S. Zhou, X. Gong, M. Cheng, R. Deng, H. Yi, Biotransformation of cadmium-sulfamethazine combined pollutant in aqueous environments: phanerochaete chrysosporium bring cautious optimism, Chem. Eng. J. 347 (2018) 74–83.
[9] R. Wang, D. Huang, Y. Liu, C. Zhang, C. Lai, G. Zeng, M. Cheng, X. Gong, J. Wan, H. Luo, Investigating the adsorption behavior and the relative distribution of Cd^{2+} sorption mechanisms on biochars by different feedstock, Bio. Technol. 261 (2018) 265–271.
[10] C. Hu, D. Huang, G. Zeng, C. Min, X. Gong, R. Wang, W. Xue, Z. Hu, Y. Liu, The combination of Fenton process and Phanerochaete chrysosporium for the removal of bisphenol A in river sediments: mechanism related to extracellular enzyme, organic acid and iron, Chem. Eng. J. 338 (2018) 432–439.

[11] W. Xue, D. Huang, G. Zeng, J. Wan, C. Zhang, R. Xu, M. Cheng, R. Deng, Nanoscale zero-valent iron coated with rhamnolipid as an effective stabilizer for immobilization of Cd and Pb in river sediments, J. Hazard. Mater. 341 (2017) 381–389.

[12] D. Huang, R. Deng, J. Wan, G. Zeng, W. Xue, X. Wen, C. Zhou, L. Hu, X. Liu, P. Xu, X. Guo, X. Ren, Remediation of lead-contaminated sediment by biochar-supported nano-chlorapatite: accompanied with the change of available phosphorus and organic matters, J. Hazard. Mater. 348 (2018) 109–116.

[13] W. Xue, D. Huang, J. Li, G. Zeng, R. Deng, Y. Yang, S. Chen, Z. Li, X. Gong, B. Li, Assembly of AgI nanoparticles and ultrathin g-C_3N_4 nanosheets codecorated Bi_2WO_6 direct dual Z-scheme photocatalyst: an efficient, sustainable and heterogeneous catalyst with enhanced photocatalytic performance, Chem. Eng. J. 373 (2019) 1144–1157.

[14] D. Huang, X. Guo, Z. Peng, G. Zeng, P. Xu, X. Gong, R. Deng, W. Xue, R. Wang, H. Yi, C. Liu, White rot fungi and advanced combined biotechnology with nanomaterials: promising tools for endocrine-disrupting compounds biotransformation, Crit. Rev. Biotechnol. 38 (2018) 671–689.

[15] D. Huang, Z. Hu, Z. Peng, G. Zeng, G. Chen, C. Zhang, M. Cheng, J. Wan, X. Wang, X. Qin, Cadmium immobilization in river sediment using stabilized nanoscale zero-valent iron with enhanced transport by polysaccharide coating, J. Environ. Manage. 210 (2018) 191–200.

[16] X. Gong, D. Huang, Y. Liu, G. Zeng, R. Wang, J. Wei, C. Huang, P. Xu, J. Wan, C. Zhang, Pyrolysis and reutilization of plant residues after phytoremediation of heavy metals contaminated sediments: for heavy metals stabilization and dye adsorption, Bio. Technol. 253 (2018) 64–71.

[17] D. Huang, X. Yan, M. Yan, G. Zeng, C. Zhou, J. Wan, M. Cheng, W. Xue, Graphitic carbon nitride-based heterojunction photoactive nanocomposites: applications and mechanism insight, ACS Appl. Mater. Interfaces 10 (2018) 21035–21055.

[18] D. Huang, S. Chen, G. Zeng, X. Gong, C. Zhou, M. Cheng, W. Xue, X. Yan, J. Li, Artificial Z-scheme photocatalytic system: what have been done and where to go? Coordin. Chem. Rev. 385 (2019) 44–80.

[19] Y. Yang, C. Zhang, C. Lai, G. Zeng, D. Huang, M. Cheng, J. Wang, F. Chen, C. Zhou, W. Xiong, BiOX (X = Cl, Br, I) photocatalytic nanomaterials: applications for fuels and environmental management, Adv. Colloid Interface Sci. 254 (2018) 76–93.

[20] D. Huang, Z. Li, G. Zeng, C. Zhou, W. Xue, X. Gong, X. Yan, S. Chen, W. Wang, M. Cheng, Megamerger in photocatalytic field: 2D g-C_3N_4 nanosheets serve as support of 0D nanomaterials for improving photocatalytic performance, Appl. Catal. B 240 (2019) 153–173.

[21] C. Zhou, C. Lai, D. Huang, G. Zeng, C. Zhang, M. Cheng, L. Hu, J. Wan, W. Xiong, M. Wen, X. Wen, L. Qin, Highly porous carbon nitride by supramolecular preassembly of monomers for photocatalytic removal of sulfamethazine under visible light driven, Appl. Catal. B 220 (2018) 202–210.

[22] Y. Yang, C. Zhang, D. Huang, G. Zeng, J. Huang, C. Lai, C. Zhou, W. Wang, H. Guo, W. Xue, R. Deng, M. Cheng, W. Xiong, Boron nitride quantum dots decorated ultrathin porous g-C_3N_4: intensified exciton dissociation and charge transfer for promoting visible-light-driven molecular oxygen activation, Appl. Catal. B 245 (2019) 87–99.

[23] L. Zhang, H. Wang, Z. Chen, P.K. Wong, J. Liu, Bi_2WO_6 micro/nano-structures: synthesis, modifications and visible-light-driven photocatalytic applications, Appl. Catal. B 106 (2011) 1–13.

[24] Q. Zhang, J. Chen, Y. Xie, M. Wang, X. Ge, Inductive effect of poly(vinyl pyrrolidone) on morphology and photocatalytic performance of Bi_2WO_6, Appl. Surf. Sci. 368 (2016) 332–340.

[25] Y. Su, G. Tan, T. Liu, L. Lv, Y. Wang, X. Zhang, Z. Yue, H. Ren, A. Xia, Photocatalytic properties of Bi_2WO_6/$BiPO_4$ Z-scheme photocatalysts induced by double internal electric fields, Appl. Surf. Sci. 457 (2018) 104–114.

[26] K. Kadeer, Y. Tursun, T. Dilinuer, K. Okitsu, A. Abulizi, Sonochemical preparation and photocatalytic properties of CdS QDs/Bi_2WO_6 3D heterojunction, Ceram. Int. 44 (2018) 13797–13805.

[27] M. Dong, J. Wu, M. Gao, Y. Xin, T. Ma, Y. Sun, Fabrication of Z-scheme g-C_3N_4/RGO/Bi_2WO_6 photocatalyst with enhanced visible-light photocatalytic activity, Chem. Eng. J. 290 (2016) 136–146.

[28] Y. Liang, S. Lin, L. Li, J. Hu, W. Cui, Oil-in-water self-assembled Ag@AgCl QDs sensitized Bi_2WO_6: enhanced photocatalytic degradation under visible light irradiation, Appl. Catal. B 164 (2015) 192–203.

[29] P. Zhou, J. Yu, M. Jaroniec, All-solid-state Z-Scheme photocatalytic systems, Adv. Mater. 26 (2014) 4920–4935.

[30] J. Low, J. Yu, M. Jaroniec, S. Wageh, A.A. Al-Ghamdi, Heterojunction photocatalysts, Adv. Mater. 29 (2017) 1601694.

[31] X. Yuan, Z. Wu, G. Zeng, L. Jiang, J. Zhang, T. Xiong, H. Wang, D. Mo, Synthesis and boosting visible light photoactivity of Ag@AgI/$CdWO_4$ towards refractory organic pollutants degradation based on interfacial charge transfer, Appl. Surf. Sci. 454 (2018) 293–304.

[32] J. Hou, Z. Wang, C. Yang, W. Zhou, S. Jiao, H. Zhu, Hierarchically Plasmonic Z-Scheme Photocatalyst of Ag/AgCl Nanocrystals decorated mesoporous single-crystalline metastable $Bi_{20}TiO_{32}$ nanosheets, J. Phys. Chem. C 117 (2013) 5132–5141.

[33] Y. Yang, Z. Zeng, C. Zhang, D. Huang, G. Zeng, R. Xiao, C. Lai, C. Zhou, H. Guo, W. Xue, Construction of iodine vacancy-rich BiOI/Ag@AgI Z-scheme heterojunction photocatalysts for visible-light-driven tetracycline degradation: transformation pathways and mechanism insight, Chem. Eng. J. 349 (2018) 808–821.

[34] C. Zhou, C. Lai, P. Xu, G. Zeng, D. Huang, C. Zhang, M. Cheng, L. Hu, J. Wan, Y. Liu, In situ grown AgI/$Bi_{12}O_{17}Cl_2$ heterojunction photocatalysts for visible light degradation of sulfamethazine: efficiency, pathway and mechanism, ACS Sustain. Chem. Eng. 6 (2018) 4147–4184.

[35] C. Sun, Y. Wang, Q. Su, Sol-gel synthesis of Bi_2WO_6/graphene thin films with enhanced photocatalytic performance for nitric monoxide oxidation under visible light irradiation, Chem. Phys. Lett. 702 (2018) 49–56.

[36] M. Zargazi, M.H. Entezari, Anodic electrophoretic deposition of Bi_2WO_6 thin film: high photocatalytic activity for degradation of a binary mixture, Appl. Catal. B. 242 (2019) 507–517.

[37] B.Y. Alfaifi, A.A. Tahir, K.G.U. Wijayantha, Fabrication of Bi_2WO_6 photoelectrodes with enhanced photoelectrochemical and photocatalytic performance, Sol. Energy Mater. Sol. Cells 195 (2019) 134–141.

[38] L. Zhang, K. Wang, Z. Chen, J. Yu, J. Zhao, C. Hu, C. Chan, P. Wong, AgBr-Ag-Bi_2WO_6 nanojunction system: a novel and efficient photocatalyst with double visible-light active components, Appl. Catal. A 363 (2009) 221–229.

[39] S. Lin, L. Liu, J. Hu, Y. Liang, W. Cui, Nano Ag@AgBr surface-sensitized Bi_2WO_6 photocatalyst: oil-in-water synthesis and enhanced photocatalytic degradation, Appl. Surf. Sc. 324 (2015) 20–29.

[40] S. Jonjana, A. Phuruangrat, S. Thongtem, T. Thongtem, Synthesis, characterization and photocatalysis of heterostructure AgBr/Bi_2WO_6 nanocomposites, Mater. Lett. 216 (2018) 92–96.

[41] X. Wen, C. Niu, H. Guo, L. Zhang, C. Liang, G. Zeng, Photocatalytic degradation of levofloxacin by ternary Ag_2CO_3/CeO_2/AgBr photocatalyst under visible-light irradiation: Degradation pathways, mineralization ability, and an accelerated interfacial charge transfer process study, J. Catal. 358 (2018) 211–223.

[42] D. Wang, Y. Zhen, G. Xue, F. Fu, X. Liu, D. Li, Synthesis of mesoporous Bi_2WO_6 architectures and their gas sensitivity to ethanol, J. Mater. Chem. C 1 (2013) 4153–4162.

[43] C. Fei, Y. Qi, S. Jian, F. Yao, S. Wang, Y. Wang, X. Wang, X. Li, C. Niu, D. Wang, Enhanced photocatalytic degradation of tetracycline by AgI/$BiVO_4$ heterojunction under visible-light irradiation: mineralization efficiency and mechanism, ACS Appl. Mater. Interfaces 8 (2016) 32887–32900.

[44] X. Li, R. Huang, Y. Hu, Y. Chen, W. Liu, R. Yuan, Z. Li, A templated method to Bi_2WO_6 hollow microspheres and their conversion to double-shell Bi_2O_3/Bi_2WO_6 hollow microspheres with improved photocatalytic performance, Inorg. Chem. 51 (2012) 6245–6250.

[45] A. Yuan, H. Lei, F. Xi, J. Liu, L. Qin, Z. Chen, X. Dong, Graphene quantum dots decorated graphitic carbon nitride nanorods for photocatalytic removal of antibiotics, J. Colloid Inter. Sci. 548 (2019) 56–65.

[46] B. Li, C. Lai, G. Zeng, L. Qin, H. Yi, D. Huang, C. Zhou, X. Liu, M. Cheng, P. Xu, C. Zhang, F. Huang, S. Liu, Facile hydrothermal synthesis of Z-Scheme $Bi_2Fe_4O_9$/Bi_2WO_6 heterojunction photocatalyst with enhanced visible light photocatalytic activity, ACS Appl. Mater. Interfaces 10 (2018) 18824–18836.

[47] B. Zhou, X. Zhao, H. Liu, J. Qu, C. Huang, Visible-light sensitive cobalt-doped $BiVO_4$ (Co-$BiVO_4$) photocatalytic composites for the degradation of methylene blue dye in dilute aqueous solutions, Appl. Catal. B 99 (2010) 214–221.

[48] C. Jiao, Z. Yang, W. Xiong, Y. Zhou, Y. Peng, X. Li, C. Zhou, R. Xu, Y. Zhang, One-step synthesis of Co-doped UiO-66 nanoparticle with enhanced removal efficiency of tetracycline: simultaneous adsorption and photocatalysis, Chem. Eng. J. 353 (2018) 126–137.

[49] J. Lyu, Z. Hu, Z. Li, M. Ge, Removal of tetracycline by BiOBr microspheres with oxygen vacancies: combination of adsorption and photocatalysis, J. Phys. Chem. Solids 129 (2019) 61–70.

[50] R. Hailili, Z. Wang, Y. Li, Y. Wang, V.K. Sharma, X. Gong, C. Wang, Oxygen vacancies induced visible-light photocatalytic activities of $CaCu_3Ti_4O_{12}$ with controllable morphologies for antibiotic degradation, Appl. Catal. B 221 (2018) 422–432.

[51] R. Shi, G. Huang, J. Lin, Y. Zhu, Photocatalytic activity enhancement for Bi_2WO_6 by fluorine substitution, J. Phys. Chem. C 113 (2009) 19633–19638.

[52] J. Cao, B. Luo, H. Lin, B. Xu, S. Chen, Visible light photocatalytic activity enhancement and mechanism of AgBr/Ag_3PO_4 hybrids for degradation of methyl orange, J. Hazard. Mater. 217–218 (2012) 107–115.

[53] E.M. Carstea, J. Bridgeman, A. Baker, D.M. Reynolds, Fluorescence spectroscopy for wastewater monitoring: a review, Water Res. 95 (2016) 205–219.

[54] W. Wang, P. Xu, M. Chen, G. Zeng, C. Zhang, C. Zhou, Y. Yang, D. Huang, C. Lai, M. Cheng, L. Hu, W. Xiong, H. Guo, M. Zhou, Alkali metal-assisted synthesis of graphite carbon nitride with tunable band-gap for enhanced visible-light-driven photocatalytic performance, ACS Sustain. Chem. Eng. 6 (2018) 15503–15516.

[55] W. Chen, P. Westerhoff, J.A. Leenheer, K. Booksh, Fluorescence excitation-emission matrix regional integration to quantify spectra for dissolved organic matter, Environ. Sci. Technol. 37 (2003) 5701–5710.

[56] F. Chen, Q. Yang, X. Li, G. Zeng, D. Wang, C. Niu, J. Zhao, H. An, T. Xie, Y. Deng, Hierarchical assembly of graphene-bridged Ag_3PO_4/Ag/$BiVO_4$ (040) Z-scheme photocatalyst: an efficient, sustainable and heterogeneous catalyst with enhanced visible-light photoactivity towards tetracycline degradation under visible light irradiation, Appl. Catal. B 200 (2017) 330–342.

[57] X. Liu, P. Lv, G. Yao, C. Ma, P. Huo, Y. Yan, Microwave-assisted synthesis of selective degradation photocatalyst by surface molecular imprinting method for the degradation of tetracycline onto Cl-TiO_2, Chem. Eng. J. 217 (2013) 398–406.

[58] Z. Zhu, Y. Yu, H. Huang, X. Yao, H. Dong, Z. Liu, Y. Yan, C. Li, P. Huo, Microwave-hydrothermal synthesis of a novel, recyclable and stable photocatalytic nanoreactor for recognition and degradation of tetracycline, Catal. Sci. Technol. 7 (2017) 4092–4104.

[59] N. Barhoumi, H. Olvera-Vargas, N. Oturan, D. Huguenot, A. Gadri, S. Ammar, E. Brillas, M.A. Oturan, Kinetics of oxidative degradation/mineralization pathways of the antibiotic tetracycline by the novel heterogeneous electro-Fenton process with solid catalyst chalcopyrite, Appl. Catal. B 209 (2017) 637–647.

[60] X. Zhu, Y. Wang, R. Sun, D. Zhou, Photocatalytic degradation of tetracycline in aqueous solution by nanosized TiO_2, Chemosphere 92 (2013) 925–932.

[61] S. Jiao, S. Zheng, D. Yin, L. Wang, L. Chen, Aqueous photolysis of tetracycline and toxicity of photolytic products to luminescent bacteria, Chemosphere 73 (2008)

377–382.
[62] Y. Ma, H. Xiong, Z. Zhao, Y. Yu, D. Zhou, S. Dong, Model-based evaluation of tetracycline hydrochloride removal and mineralization in an intimately coupled photocatalysis and biodegradation reactor, Chem. Eng. J. 351 (2018) 967–975.
[63] T. Soltani, A. Tayyebi, B.K. Lee, Photolysis and photocatalysis of tetracycline by sonochemically heterojunctioned $BiVO_4$/reduced graphene oxide under visible-light irradiation, J. Environ. Manage. 232 (2019) 713–721.
[64] C. Zhang, K. Yu, Y. Feng, Y. Chang, T. Yang, Y. Xuan, D. Lei, L. Lou, S. Liu, Novel 3DOM-$SrTiO_3$/Ag/Ag_3PO_4 ternary Z-scheme photocatalysts with remarkably improved activity and durability for contaminant degradation, Appl. Catal. B 210 (2017) 77–87.
[65] C. Liang, C. Niu, H. Guo, D. Huang, X. Wen, S. Yang, G. Zeng, Combination of efficient charge-separation process with the assistance of novel dual Z-scheme system: self-assembly photocatalyst of Ag@AgI/BiOI modified oxygen-doped carbon nitride nanosheet with enhanced photocatalytic performance, Catal. Sci. Technol. 8 (2018) 1161–1175.